

## PAPER

# Bifunctional pyrazolate–carboxylate ligands for isorecticular cobalt and zinc MOF-5 analogs with magnetic analysis of the $\{Co_4(\mu_4-O)\}$ node†‡

Cite this: *CrystEngComm*, 2013, 15, 9757

Christian Heering,<sup>a</sup> Ishtvan Boldog,<sup>a</sup> Vera Vasylyeva,<sup>a</sup> Joaquín Sanchiz<sup>\*b</sup> and Christoph Janiak<sup>\*a</sup>

The ditopic ligands 3,5-dimethyl-pyrazolate-4-carboxylate,  $^-Me_2pzCO_2^-$ , and 4-(3,5-dimethyl-1*H*-pyrazol-4-yl)benzoate,  $^-Me_2pzC_6H_4CO_2^-$ , combine a pyrazolate and carboxylate functionality in axial orientation and lead to porous cobalt or zinc azolate–carboxylate frameworks that have the same cubic *pcu-a* topology and  $\{M_4(\mu_4-O)\}$  nodes ( $M = Co, Zn$ ) as MOF-5 and other IRMOFs. The microporous networks  $[M_4(\mu_4-O)(Me_2pzCO_2)_3]$  ( $M = Co, Zn$ ) with the short linker exhibit a solvent-induced gate effect, evidenced by gas desorption hysteresis due to small pore apertures of 2.8 Å diameter together with small amounts of high-boiling solvent remaining in the activated samples. For  $[Co_4(\mu_4-O)(Me_2pzCO_2)_3]$ , the low-pressure  $H_2$  storage capacity (1.7 wt%, 1 bar, 77 K) is higher than for MOF-5, and the  $CO_2$  uptake of 20.8 wt% puts it among the top MOFs for low-pressure  $CO_2$  sorption even though the BET surface is less than  $1000\text{ m}^2\text{ g}^{-1}$ . The analysis of the magnetic properties of  $[Co_4(\mu_4-O)(Me_2pzCO_2)_3]$  takes into account the distribution of tetrahedra resulting from the disorder of the pyrazolate–carboxylate linker. An antiferromagnetic coupling observed for  $[Co_4(\mu_4-O)(Me_2pzCO_2)_3]$  arises from the interactions of the cobalt(II) ions through the combined  $\mu_4-O + syn-syn$  carboxylate and  $\mu_4-O + pyrazolate$  bridges.

Received 18th July 2013,

Accepted 16th August 2013

DOI: 10.1039/c3ce41426d

www.rsc.org/crystengcomm

## Introduction

Metal–organic frameworks (MOFs) receive continuous attention<sup>1,2</sup> due to their high porosity that promises applications such as gas storage,<sup>3,4</sup> gas<sup>5,6</sup> and liquid<sup>7</sup> separation processes, drug delivery,<sup>8</sup> heterogeneous catalysis,<sup>9</sup> heat transformation,<sup>10</sup> etc.

Isorecticular (IR) MOFs with linear dicarboxylate linkers ( $^-O_2C-R-CO_2^-$ ) and the  $\{Zn_4O(O_2CR)_6\}$  secondary building unit are attractive in their predictable design of the same *pcu-a* primitive cubic network featuring high surface areas and wide 3-D channel porosity.<sup>12,13</sup> MOF-5,  $[Zn_4O(BDC)_3]$  (BDC = benzene-1,4-dicarboxylate, terephthalate), is one of the best known MOFs,<sup>14</sup> has a high surface area ( $3000\text{ m}^2\text{ g}^{-1}$ ) and has high thermal stability (up to  $400\text{ }^\circ\text{C}$ )<sup>12</sup> but low water stability.<sup>15,16</sup> Many MOFs cannot withstand prolonged contact with water or moisture at room temperature.<sup>16</sup> This is due to the

hydrolysis of coordination bonds and often limits the practical use of these materials. Only a few MOFs have had their moisture/water stability proven with retention of porosity.<sup>10,17,18</sup> The development of hydrolytically stable MOFs is one important goal to advance MOFs to the application stage.<sup>5,17</sup> One of the most hydrolytically stable MOFs is ZIF-8,  $[Zn(2\text{-methylimidazolate})_2]_n$ ,<sup>16,19</sup> which is stable in boiling water over a broad pH range, excluding only strongly alkaline conditions, and exceeds MIL-101<sup>20</sup> and UiO-66.<sup>21</sup> The hydrolytic stability of ZIF-8 can be associated with the greater basicity of the imidazolate linker, leading to higher covalency of the metal-to-azolate bonds<sup>22</sup> compared to carboxylates and with higher hydrophobicity of the ZIF-8 framework. Recent advances in pyrazolate MOFs<sup>23</sup> by Masciocchi, Navarro, Bordiga,<sup>24</sup> Long,<sup>22</sup> and Volkmer (MFU-1,2)<sup>25</sup> prove the high hydrolytic stability of novel hydrophobic bis-pyrazolate MOFs.<sup>26</sup>

There are few but promising reports on the utilization of bifunctional pyrazolate–carboxylate linkers. The 4-pyrazolate–carboxylate linker  $^-pzCO_2^-$  has been employed in the synthesis of MOF-325 with  $\{Cu_2(O_2C)_4\}$  paddle wheel and trinuclear pyramidal  $\{Cu_3(\mu_3-O)(pz)_3\}$  units as nodes.<sup>27</sup> A related 4-triazolate–carboxylate linker  $^-tzCO_2^-$  gave the double-walled metal triazolate framework, MTAF-1, material with pentanuclear zinc clusters  $\{Zn_5(\mu_3-O)(tz)_5(O_2C)_5\}$ .<sup>28</sup> A porous metal azolate framework MAF-X8 has been reported with the 4-(3,5-dimethyl-pyrazolate)benzoate linker with one-dimensional

<sup>a</sup> Institut für Anorganische Chemie und Strukturchemie, Heinrich-Heine Universität Düsseldorf, Universitätsstraße 1, D-40225 Düsseldorf, Germany. E-mail: janiak@uni-duesseldorf.de

<sup>b</sup> Departamento de Química Inorgánica, Facultad de Química, C/ Astrofísico Francisco Sánchez s/n, La Laguna 38206, Tenerife, Spain. E-mail: jsanchiz@ull.es

† Electronic supplementary information (ESI) available: Details of syntheses and spectroscopic analysis, thermogravimetric and sorption studies. CCDC 937761–937763. For ESI and crystallographic data in CIF or other electronic format see DOI: 10.1039/c3ce41426d

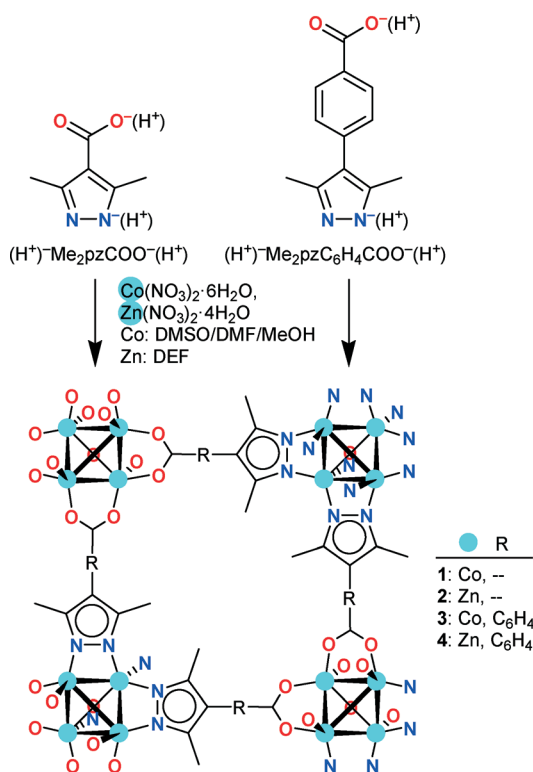
‡ Dedicated to Prof. Dr. Bernt Krebs on the occasion of his 75<sup>th</sup> birthday.

channels and  $\text{Zn}(\mu\text{-O}_2\text{C})(\mu\text{-pz})$  chains.<sup>29</sup> The 1,2,4-triazol-4-yl-isophthalate linker contains a neutral azole but also yields multinuclear copper and cobalt nodes in microporous MOFs.<sup>30</sup> A MOF-5 analog has been reported with the 3,5-dimethyl-pyrazolate-4-carboxylate linker  $\text{Me}_2\text{pzCO}_2^-$  (Scheme 1) crystal and shown to exhibit remarkable hydrolytic, thermal, mechanical, and chemical stability.<sup>31,32</sup> The hydrolytic stability of the  $[\text{Zn}_4(\mu_4\text{-O})(\text{Me}_2\text{pzCO}_2)_3]$  framework was traced to its hydrophobic nature. The ligands  $\text{pzCO}_2^-$  and  $\text{pzC}_6\text{H}_4\text{CO}_2^-$  (*cf.* the ligands in Scheme 1 without the methyl groups) yielded isorecticular  $[\text{Ni}_8(\text{OH})_4(\text{H}_2\text{O})_2(\text{L})_6]$  frameworks.<sup>26</sup>

Here we utilize the two rigid linear ligands  $\text{Me}_2\text{pzCO}_2^-$  and  $\text{Me}_2\text{pzC}_6\text{H}_4\text{CO}_2^-$  with combined but differently spaced azolate and carboxylate functionality to assess the isorecticular principle for the synthesis of microporous Metal-Azolate-Carboxylate (MAC) frameworks with cobalt and zinc (Scheme 1).

## Results and discussion

Solvothermal reaction of cobalt or zinc nitrate with 3,5-dimethyl-1*H*-pyrazole-4-carboxylic acid ( $\text{HMe}_2\text{pzCO}_2\text{H}$ ) or 4-(3,5-dimethyl-1*H*-pyrazol-4-yl)benzoic acid ( $\text{HMe}_2\text{pzC}_6\text{H}_4\text{CO}_2\text{H}$ ) yields small blue-violet (Co) or yellowish (Zn) crystals of cubic shape (Scheme 1, Fig. 1) (see ESI† for full syntheses details). Previously,  $[\text{Zn}_4(\mu_4\text{-O})(\text{Me}_2\text{pzCO}_2)_3]$  (2) was prepared in a basic ethanol medium as a microcrystalline material



**Scheme 1** Bifunctional pyrazolate-carboxylate ligands and derived cubic metal-azolate-carboxylate frameworks (extension into the third dimension is not shown for clarity, *cf.* Fig. 1). Note that the edges of the tetrahedral  $\{\text{M}_4(\mu_4\text{-O})\}$  nodes will be statistically bridged by both carboxylate or pyrazolate groups as indicated in the lower half of the sketched framework (*cf.* Fig. 9).

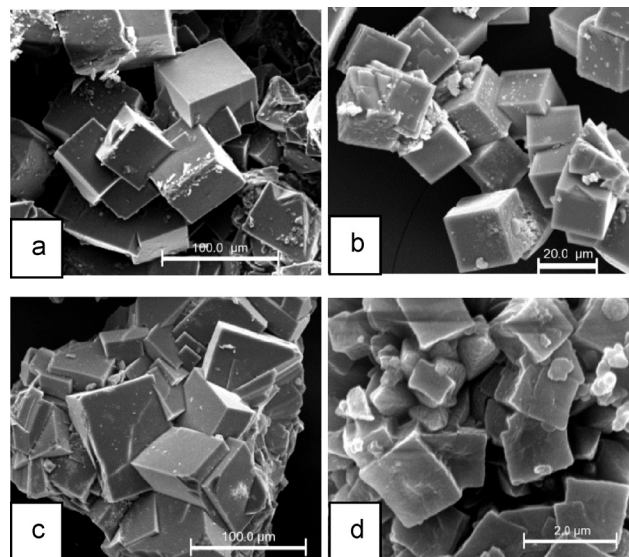


**Fig. 1** Scanning electron micrographs of (a) 1, (b) 2, (c) 3 and (d) 4. The cubic morphology of 1 and 2 (cubic space group  $F\bar{4}3m$ ) is identical to MOF-5 (cubic space group  $Fm\bar{3}m$ ).<sup>11</sup> For color photographs of crystals and additional SEM pictures, see ESI.†

from which the structure was obtained by Rietveld refinement.<sup>31</sup> Here we used a solvent mixture (DMSO, DMF, and MeOH) for the Co analog 1 or DEF alone for 2 to obtain  $[\text{M}_4(\mu_4\text{-O})(\text{Me}_2\text{pzCO}_2)_3]$  ( $\text{M} = \text{Co}, \text{Zn}$ ) as single crystals, which were also susceptible to single-crystal X-ray diffraction analysis.

### Solid-state structural studies

Compounds of Co (1) and Zn (2) with the short pyrazolate-carboxylate linker are isostructural (*cf.* Table 2) and of the same cubic topology and have the same tetrahedral  $\{\text{M}_4(\mu_4\text{-O})(\text{pz}/\text{O}_2\text{C})_3\}$  node ( $\text{M} = \text{Co}, \text{Zn}$ ) as in MOF-5 (Fig. 2, Fig. S23 in ESI†). The previous Rietveld refinement of compound 2 gave the cubic space group  $Fm\bar{3}m$ .<sup>31</sup> The six edges of the oxido-metal tetrahedron  $\{\text{M}_4(\mu_4\text{-O})\}$  are bridged by either the carboxylate or the pyrazolate group of the ligand. Each 3,5-dimethyl-pyrazolate-4-carboxylate ligand bridges between two  $\{\text{M}_4(\mu_4\text{-O})\}$  clusters, just like the terephthalate ligand in MOF-5.

The pyrazolate-carboxylate ligand is disordered (Fig. 2a), and each  $\{\text{M}_4(\mu_4\text{-O})\}$  cluster has a mixed pyrazolate/carboxylate coordination environment (*cf.* Fig. 9). The fixed alternating canting of the dimethylpyrazolate ring plane (Fig. 2a) leads to alternating small (van der Waals diameter,  $\text{O} \sim 6 \text{ \AA}$ ) and large pores ( $\text{O} \sim 11 \text{ \AA}$ ) connected by small channels or pore apertures ( $\text{O} \sim 2.8 \text{ \AA}$ ) (Fig. 2c).

Frameworks of Co (3) and Zn (4) with the long pyrazolate-benzoate ligand are also isostructural to each other (by X-ray powder diffraction, *cf.* Fig. S26†) and again of near cubic topology and with the tetrahedral  $\{\text{M}_4(\mu_4\text{-O})(\text{pz}/\text{O}_2\text{C})_3\}$  node ( $\text{M} = \text{Co}, \text{Zn}$ ) as in carboxylate IRMOFs<sup>12</sup> (Fig. 3). Thus, elongation of rigid bifunctional pyrazolate-carboxylate linkers appears to follow the isorecticular principle.<sup>12</sup>

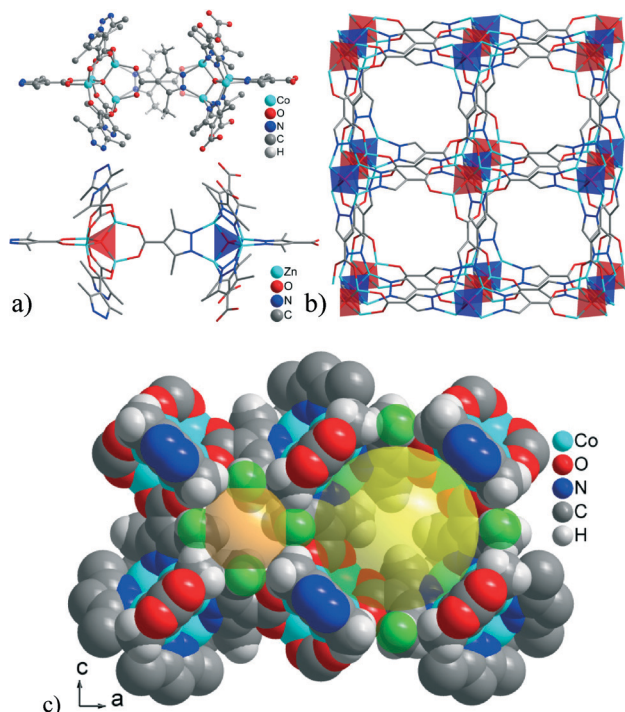


**Fig. 2** Building unit (a) and framework (b) in  $[M_4(\mu_4\text{-O})(\text{Me}_2\text{pzCOO})_3]$  ( $M = \text{Co}$ , **1**;  $\text{Zn}$ , **2**) as MOF-5-analogs with the pyrazolate-carboxylate ligand (*cf.* Scheme 1). The central ligand in (a) illustrates the ligand disorder. For graphic simplicity, an idealized pyrazolate-only and carboxylate-only coordination for alternating  $\{M_4O\}$  clusters in the framework (b) is depicted with all-oxygen coordination as red and all-nitrogen coordination as blue tetrahedra; methyl groups and hydrogen atoms are not shown in (b). A space-filling plot in (c) shows the alternating small (transparent orange sphere, diameter,  $\varnothing = 6 \text{ \AA}$ ) and large (yellow sphere,  $\varnothing = 11 \text{ \AA}$ ) cavities due to the alternating pyrazolate plane orientation with pore apertures (green spheres,  $\varnothing = 2.8 \text{ \AA}$ ) in between.

We note that numerous crystallization experiments to obtain single crystals of **3** of suitable large size gave at best crystals of about  $0.01 \times 0.01 \times 0.01 \text{ mm}$ , which were at the manageable limit for an X-ray diffractometer even when equipped with a microfocus source. Still, a representative X-ray data set could be obtained for **3**, even though the small crystal size and high absorption coefficient of Co atoms limited the  $2\theta$  angle to  $80^\circ$  for Cu-K $\alpha$  radiation and the data set quality.

### Porosity and gas sorption

According to the X-ray structure (*cf.* Fig. 2, Fig. S24<sup>†</sup>), the pore openings in the isostructural compounds **1** and **2** are very narrow. Thus, the traditional solvent exchange procedure, through soaking in a low-boiling solvent (like MeOH,  $\text{CH}_2\text{Cl}_2$ ), was regarded ineffective. Hence, activation of **1** and **2** was carried out by direct high-temperature degassing. The thermogravimetric (TG) analyses of **1** and **2** (Fig. S13 and S16,<sup>†</sup> respectively) revealed that complete loss of solvent guest molecules should be finished at temperatures of  $\sim 300\text{--}350 \text{ }^\circ\text{C}$  at atmospheric pressure. Samples of **1** were degassed at different temperatures in  $\sim 10^{-6}$  bar vacuum, and  $\text{H}_2$  adsorption was measured in order to determine the optimum degassing conditions for both **1** and

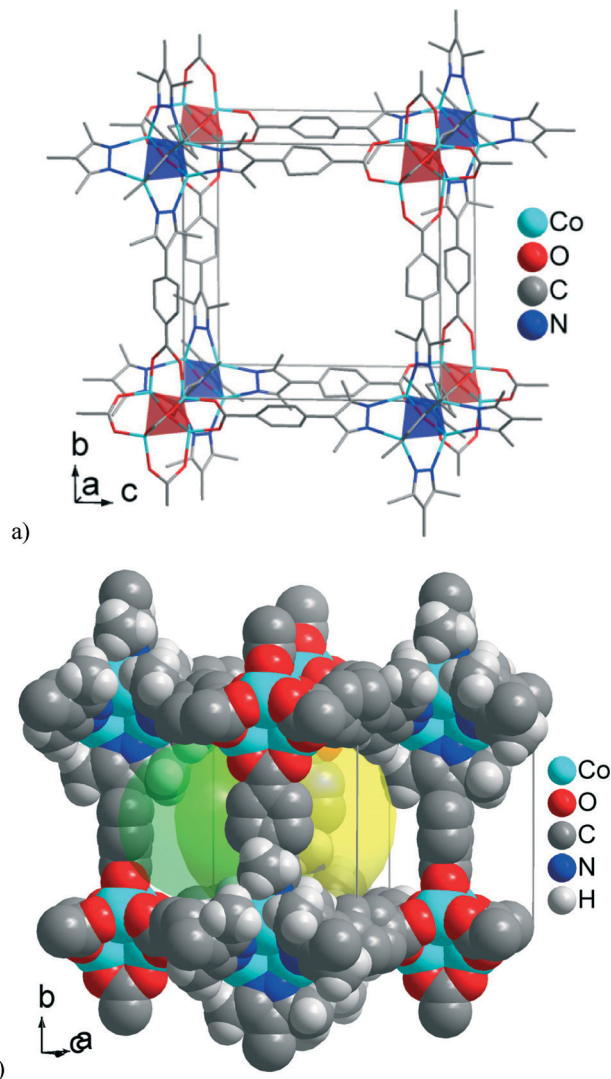


**Fig. 3** (a) Framework in  $[M_4(\mu_4\text{-O})(\text{Me}_2\text{pzC}_6\text{H}_4\text{CO}_2)_3]$  ( $M = \text{Co}$ , **3**;  $\text{Zn}$ , **4**) as IRMOF analogs with the pyrazolate-benzoate ligand (*cf.* Scheme 1). The ligands are crystallographically disordered by a  $C_2$  symmetry operation, which is detailed in Fig. S25.<sup>†</sup> An idealized pyrazolate-only (blue) and carboxylate-only (red tetrahedra) coordination for  $\{M_4O\}$  clusters is depicted. (b) Space-filling plot for **3** showing the large cavity (yellow transparent sphere,  $\varnothing = 14 \text{ \AA}$ ) and one of the pore apertures (green transparent sphere,  $\varnothing = 10 \text{ \AA}$ ).

**2**. For **1** degassed at  $190 \text{ }^\circ\text{C}$ , an  $\text{H}_2$  adsorption of  $145 \text{ cm}^3 \text{ g}^{-1}$  at STP (standard temperature and pressure) was found; at  $220 \text{ }^\circ\text{C}$ , an  $\text{H}_2$  adsorption of  $188 \text{ cm}^3 \text{ g}^{-1}$  was observed; and at  $250 \text{ }^\circ\text{C}$ , an  $\text{H}_2$  adsorption of  $193 \text{ cm}^3 \text{ g}^{-1}$  was obtained (*cf.* Fig. 5). TG analysis of a sample degassed at a temperature of  $250 \text{ }^\circ\text{C}$  confirmed the complete removal of guest molecules, and this degassing condition was used for subsequent gas sorption measurements for both **1** and **2**. Still,  $\text{N}_2$  is not adsorbed even on these optimally degassed samples of **1** and **2** at  $77 \text{ K}$ . This is presumably due to activated diffusion effects associated with the low thermal energy of  $\text{N}_2$  relative to the high barrier for diffusion through the small  $2.8 \text{ \AA}$  diameter pore apertures (*cf.* Fig. 2c). In other words, at slow thermal motion at  $77 \text{ K}$ , the  $\text{N}_2$  molecule will statistically only seldom approach the small

pore aperture with the correct orientation for penetration, that is, at right angle with its molecule axis. It is a frequently encountered phenomenon of kinetic hindrance of small pores or pore aperture windows (*cf.* Fig. S24†) that N<sub>2</sub> adsorption (kinetic diameter, 3.64 Å) at 77 K does not occur, while H<sub>2</sub> at 77 K or CO<sub>2</sub> at 273 K is adsorbed (see below).<sup>33</sup> Therefore, argon sorption experiments at 87 K were carried out for an experimental surface area determination of **1** (Ar diameter, 3.4 Å) (Fig. 4). The start of the argon adsorption branch for **1** is very steep and follows a type I isotherm with most of the argon adsorbed below 0.05  $P/P_0$  (Fig. 4a). The adsorption at higher relative pressure is irreversible due to small pore openings, which gives rise to an open-loop hysteresis because of a gate effect (see below). BET and Langmuir surface areas were found to be 760 and 840 m<sup>2</sup> g<sup>-1</sup>, respectively (from 0.02 <  $P/P_0$  < 0.1), with 0.32 cm<sup>3</sup> g<sup>-1</sup> pore volume (at  $P/P_0 = 0.95$ ). A DFT calculation gave a narrow pore diameter distribution with the maximum at ~12 Å (Fig. 4b) in good agreement with the cavity diameter of ~11 Å from the structural data (Fig. S24†).

For the microcrystalline zinc compound **2**, which was previously synthesized in basic ethanol, a BET surface area of 840 m<sup>2</sup> g<sup>-1</sup> together with a micropore volume of 0.45 cm<sup>3</sup> per cm<sup>3</sup> of **2** had been reported from an N<sub>2</sub> adsorption isotherm

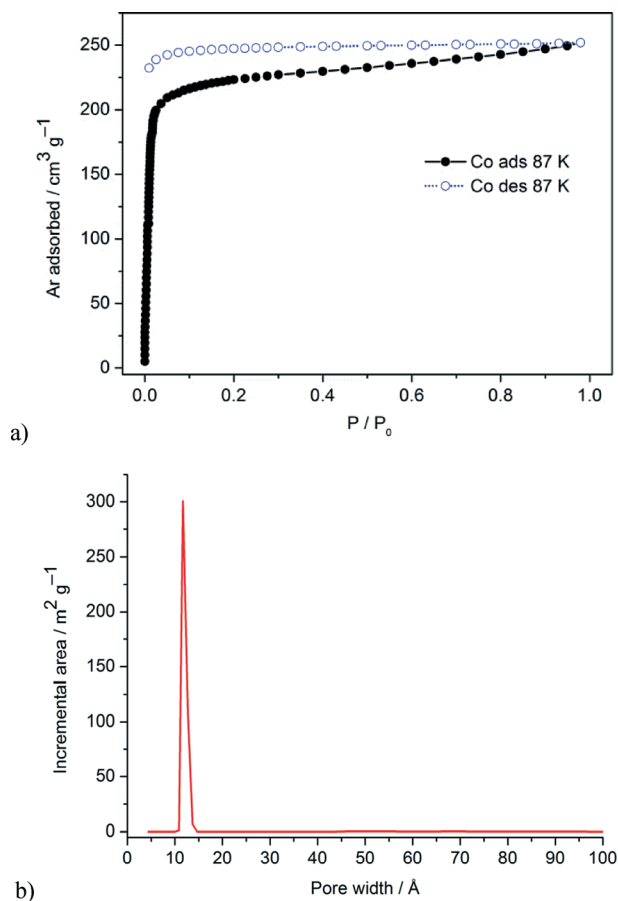


**Fig. 4** (a) Argon sorption isotherms and (b) pore size distribution curve from DFT calculation (Ar on carbon, slit based model) based on argon adsorption isotherm for **1**.

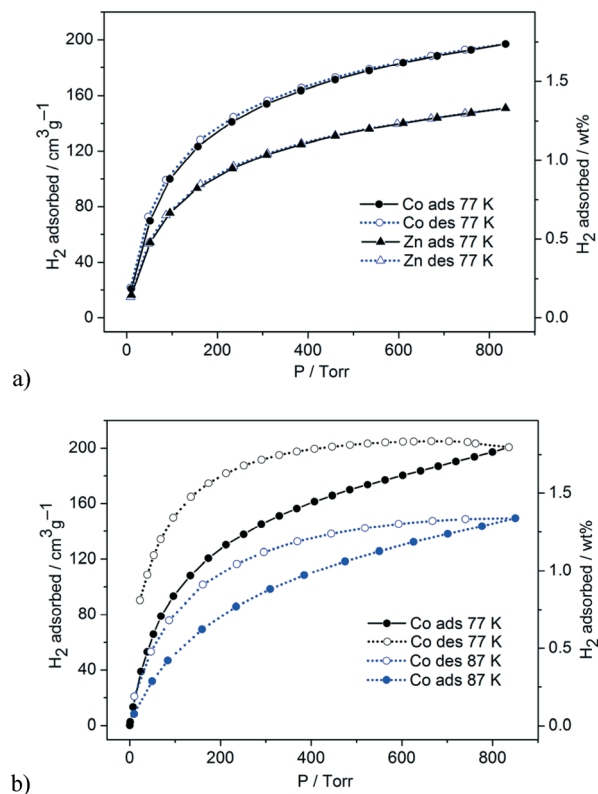


**Fig. 5** (a) Hydrogen sorption isotherms for **1** (Co) and **2** (Zn) at 77 K. The samples were degassed at 250 °C for 10 h (Co) and 220 °C for 15 h (Zn) until the pressure rise rate was approximately 3  $\mu\text{Torr min}^{-1}$ . No significant additional weight loss was registered. (b) Hydrogen sorption isotherms for **1** at 77 K and 87 K. Note the hysteresis due to hindered desorption. A similar type of broad desorption hysteresis was observed in NOTT-200.<sup>36</sup> The maximum amount of adsorbed H<sub>2</sub> at ~1.1 bar of 200 cm<sup>3</sup> g<sup>-1</sup> corresponds to 1.75 wt%.

at 77 K.<sup>31</sup> The similar surface area for **1** and **2** suggests an optimal degassing of **1**. We considered a different N<sub>2</sub> adsorption behavior at 77 K for the larger crystallite size of **1** and **2** from the solvothermal synthesis conditions of our samples. In the larger crystals, the thermodynamic adsorption equilibrium may take a longer time to be reached because of the small pore apertures ( $\varnothing = 2.8$  Å, *cf.* Fig. 2). We note that the sorption isotherms can deviate from ideal equilibrium experiments as pronounced kinetic effects occur because of the small channel size. Such effects were even seen in the case of H<sub>2</sub> sorption (kinetic diameter, 2.9 Å), depending on the sample preparation. We already stated that sorption studies with H<sub>2</sub> indicated that a larger amount of gas was adsorbed as degassing temperatures were increased, and therefore, a larger pore volume became accessible for guest molecules. Furthermore, samples used for H<sub>2</sub> sorption after long (10–15 h) degassing time did not display a hysteresis (Fig. 5a), while samples with shorter degassing time (2 h) featured a desorption hysteresis (Fig. 5b) even though the maximum amount of adsorbed H<sub>2</sub> at ~1.1 bar is identical (200 cm<sup>3</sup> g<sup>-1</sup> or 1.75 wt%). We trace this to channel blocking by residual solvent molecules as a solvent guest-induced gate effect. Normally, a gate effect is associated with structural flexibility in a MOF, with the guest

Table 1 H<sub>2</sub>, CO<sub>2</sub> and CH<sub>4</sub> uptake of 1 and 2 at 1 bar

Compd	H <sub>2</sub> <sup>a</sup> /	CO <sub>2</sub> <sup>b</sup>		CH <sub>4</sub> <sup>b</sup>	
	wt%	cm <sup>3</sup> g <sup>-1</sup> /mmol g <sup>-1</sup>	g g <sup>-1</sup> /wt%	cm <sup>3</sup> g <sup>-1</sup> /mmol g <sup>-1</sup>	g g <sup>-1</sup> /wt%
1	1.70	134.4/5.5	0.26/20.8	41.1/1.8	0.03/2.9
2	1.35	84.4/3.46	0.16/14.3	26.0/1.1	0.02/1.9

<sup>a</sup> H<sub>2</sub> uptake at 77 K. <sup>b</sup> Gas uptake at 273 K.

causing the closed–open structural transformation.<sup>34</sup> Also, flexible side groups on the linker can act as molecular gates for guest molecules in MOFs.<sup>35</sup>

The gravimetric H<sub>2</sub> storage capacity of 1.7 wt% in 1 and 1.35 wt% in 2 at 1 bar (Table 1) is higher than or equal to values in many reports for MOF-5 (1.15–1.35 wt% at 1 bar, 77 K, BET surface area of 2885–3362 m<sup>2</sup> g<sup>-1</sup>) and other higher surface area MOFs.<sup>3b</sup> From two adsorption isotherms acquired at different temperatures (Fig. 5b), the differential heat of adsorption  $\Delta H_{\text{ads,diff}}$  in 1 is determined to be 5–6 kJ mol<sup>-1</sup> (see ESI†).  $\Delta H_{\text{ads,diff}}$  for H<sub>2</sub> in 1 is higher than for MOF-5 (3.8–4.8 kJ mol<sup>-1</sup>) and ZIF-8 (4.5 kJ mol<sup>-1</sup>),<sup>3b</sup> which is traced to the small pore and channel size in 1. While N<sub>2</sub> is not adsorbed at 77 K, CO<sub>2</sub> and CH<sub>4</sub> are adsorbed at 273 K (Table 1, Fig. S30†). The CO<sub>2</sub> adsorption capacity of 20.8 wt% puts 1 among the top MOFs for low pressure CO<sub>2</sub> sorption, exceeding the values for most Zn–carboxylate MOFs.<sup>5a,37</sup>

We suggest that the passage of CO<sub>2</sub> and CH<sub>4</sub> guest molecules (kinetic diameters, 3.3 and 3.8 Å, respectively) in and out of the cavities through the pore apertures of ~2.8 Å diameter proceeds by a temporary expansion of the window size.<sup>38,39</sup> The selectivity for CO<sub>2</sub> over CH<sub>4</sub> (Table S2†) can be ascribed to the combined effects of the size of the pore apertures and the strong quadrupolar interactions of CO<sub>2</sub> with nitrogen atoms present on the pore surface. The quadrupole moment of CO<sub>2</sub> (CO<sub>2</sub>: 14.3 × 10<sup>-40</sup> cm<sup>2</sup>, N<sub>2</sub>: 4.65 × 10<sup>-40</sup> cm<sup>2</sup>, CH<sub>4</sub>: none)<sup>40</sup> leads to a stronger electrostatic interaction with the framework and can have a distinct effect on framework flexibility in that it induces a dynamic window-widening process through a concerted ligand tilt to allow gas molecules to pass.<sup>3,5</sup> The cobalt framework 1 consistently exhibits a higher gas uptake than the zinc framework 2 (Table 1, Fig. 5, and Fig. S30†). Both frameworks are isostructural with essentially identical estimated pore volumes and apertures from the X-ray structure. We have to assign the higher sorption capacity of 1 to its easier and better activation in line with the thermogravimetric analyses (see Fig. S13 and S16 in ESI†).

The MAC frameworks 3 and 4 with the longer pyrazolate–benzoate were able to adsorb N<sub>2</sub> at 77 K with a type I isotherm for microporous materials (Fig. 6, Fig. S31†). From these, the BET surfaces were calculated to be 1072 m<sup>2</sup> g<sup>-1</sup> for the cobalt compound 3 and 980 m<sup>2</sup> g<sup>-1</sup> for the zinc compound 4 (Table S1†).

### Water stability

Water and chemical stability of compound 2 was investigated in the work by Montoro *et al.* because of the sought practical

applications.<sup>31</sup> Stabilities were tested by suspending 2 in water at room temperature and in boiling benzene or MeOH for 24 h. No changes were noticed when comparing the powder X-ray diffractograms to the as-synthesized sample of 2. Also, thermogravimetric measurements in air indicated thermal robustness of 2, with decomposition beginning only at 773 K.<sup>31</sup> Montoro *et al.* also found that H<sub>2</sub>O adsorption in 2 at 298 K takes place only at very high relative pressures ( $P/P_0 > 0.7$ ), which is indicative of a highly hydrophobic nature of the material to which they assign the overall water stability.<sup>31</sup>

Cychosz and Matzger argued convincingly that it is important to assess water stability in the liquid phase explicitly.<sup>17</sup> Previous studies on MOF water stability have focused on exposure to water in the gas phase. Yet, it has been shown in the literature that gas phase adsorption is not a good predictor for liquid phase behavior.<sup>7,41</sup> Cychosz and Matzger tested the effect of water concentration for a series of MOFs. Powder X-ray diffraction (PXRD) was used to determine if the structure remains untransformed with increasing water concentration or at what water concentration the structure began to change. In a typical experiment, the as-synthesized MCP was placed in fresh DMF and defined aliquots of deionized water were added to the solution sequentially. Between aliquots, the mixture was agitated at room temperature on a shaker for 1 h.<sup>17</sup> We decided to follow this protocol to test the water stability of 1–4 (Fig. 7).

A water stability test<sup>17</sup> of the zinc complexes 2 and 4 in comparison to MOF-5 revealed a higher stability for the pyrazolate–carboxylate frameworks. Immersing crystals in a different mixture of water–DMF for 1 h did not show any structural changes by powder X-ray diffraction (Fig. 7), while for MOF-5, a

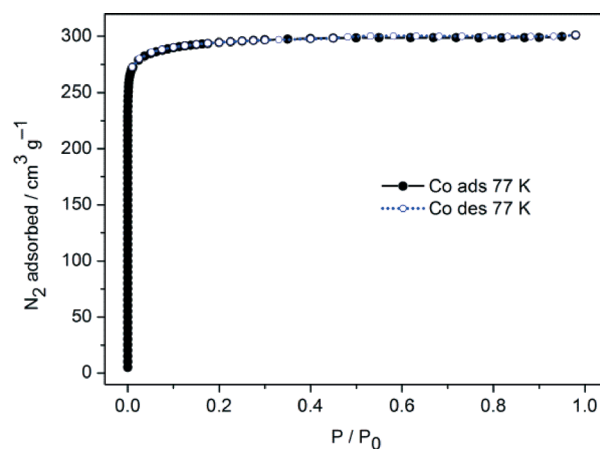
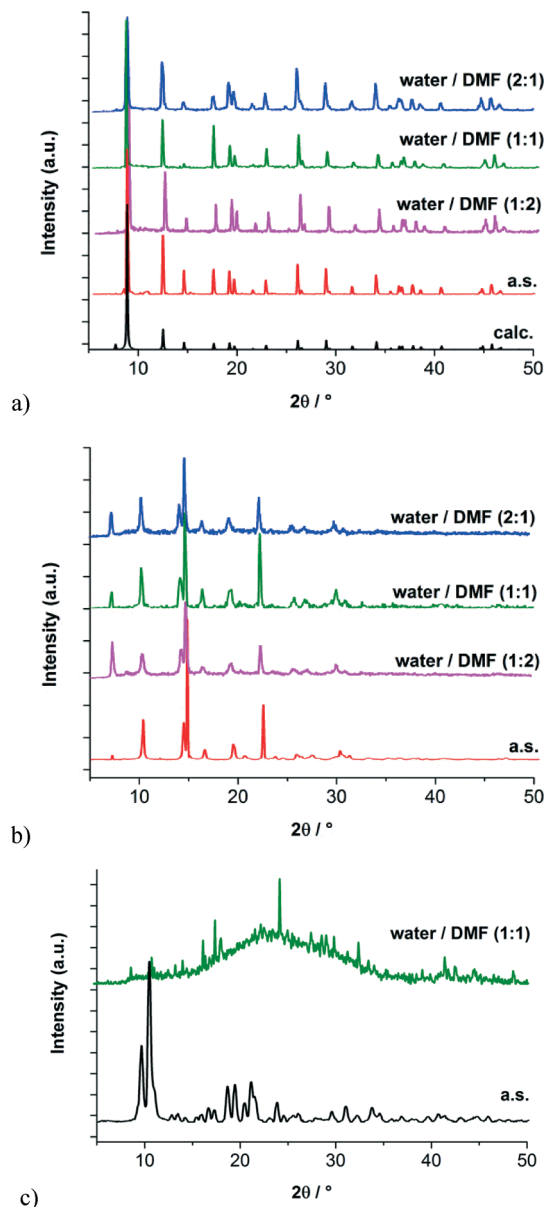


Fig. 6 N<sub>2</sub> sorption isotherms for 3.



**Fig. 7** Water stability tests by comparison of powder X-ray diffraction patterns of (a) **2**, (b) **4** and (c) MOF-5 (calc = calculated from single-crystal data, a.s. = as synthesized and after 1 hour treatment with water/DMF at different  $v : v$  ratios).

ratio of 1:<4 (water-DMF) already induced hydrolysis (Fig. 7c).<sup>17</sup> In comparison, the same hydrophobic network with cobalt in compound **1** showed pronounced decomposition after 1 h in a 1:1 water-DMF mixture (Fig. S27 in ESI†). This indicates that the hydrophobic nature of the framework alone will not prevent hydrolysis if the metal-ligand bonds are sufficiently labile. Thermogravimetric analysis shows that framework decomposition starts only above 350–400 °C (Fig. S13, S16, S19 and S22 in ESI†).

### Magnetic properties of **1**

The magnetic properties of MOFs and coordination polymers are of continuous interest.<sup>2,42–44</sup> The ground state of Co(II) ions ( $d^7$ ) in a tetrahedral environment is  $^4A_2$ , for which the orbital angular momentum contribution is a second-order effect, and so, the spin-only model can be used to describe the magnetic behaviour of compound **1**.<sup>45</sup> Fig. 8 shows the temperature dependence of the  $\chi_M T$  product for **1**. At room temperature, the  $\chi_M T$  product has a value of almost  $5.0 \text{ cm}^3 \text{ mol}^{-1} \text{ K}$ , which is lower than expected for four isolated spin quartets, and it continuously decreases on lowering temperature, reaching a value of  $0.50 \text{ cm}^3 \text{ mol}^{-1} \text{ K}$  at 2.0 K (the value expected at room temperature in the spin-only model for four cobalt(II) ions is  $4 \times (N\beta^2 g^2 / 3kT) S(S+1) = 9.075 \text{ cm}^3 \text{ mol}^{-1} \text{ K}$  with  $g = 2.2$  and  $S = 3/2$ ). The behavior shown is indicative of a dominant antiferromagnetic interaction in compound **1**.

According to the tetrahedral structure of the  $\{\text{Co}_4(\mu_4\text{-O})\}$  clusters, as a first approach, the magnetic properties are investigated by means of an isotropic Heisenberg-Dirac-Van Vleck Hamiltonian formalism, in which  $J$  is the exchange coupling constant and  $\hat{S}_i$  the spin operator of the centre  $i$  (eqn (1)).

$$\hat{H}_{\text{HDVV}} = -J(\hat{S}_1\hat{S}_2 + \hat{S}_1\hat{S}_3 + \hat{S}_1\hat{S}_4 + \hat{S}_2\hat{S}_3 + \hat{S}_2\hat{S}_4 + \hat{S}_3\hat{S}_4) \quad (1)$$

In this model, all the tetrahedra are considered to be equivalents, and so the coupling through the pyrazolate and through the *syn-syn* carboxylate groups is assumed to be identical (which is a rough approximation). The Eigenvalues for such a system can be obtained with the following coupling scheme in which  $S_A = S_1 + S_2$ ,  $S_B = S_3 + S_4$ ,  $S = S_A + S_B$  and  $S_1 = S_2 = S_3 = S_4 = 3/2$  (eqn (2)).

$$E = -\frac{J}{2} \left[ S(S+1) - \sum_{i=1}^4 S_i(S_i+1) \right] \quad (2)$$

The splitting of the energy levels, the degeneracy and the corresponding spin are shown in Fig. 8b, and the equation (eqn (3)) for the susceptibility is then

$$x = (N\beta^2 g^2 / (3kT)) \left[ \frac{54e^{J/kT} + 330e^{3J/kT} + 840e^{6J/kT} + 1080e^{10J/kT} + 990e^{15J/kT} + 546e^{21J/kT}}{4 + 27e^{J/kT} + 55e^{3J/kT} + 70e^{6J/kT} + 54e^{10J/kT} + 33e^{15J/kT} + 13e^{21J/kT}} \right] \quad (3)$$

The best-fit parameters to this model are  $J = -14.70 \text{ cm}^{-1}$ ,  $g = 1.84$ , and  $R = 1.22 \times 10^{-2}$ , and it can be seen that the theoretical plot does not match very well with the experimental values, and the value of  $g$  is lower than expected.<sup>46</sup> The reason for the deviation is evidently the fact that the pyrazolate and *syn-syn* carboxylate bridges mediate, in a different way, the magnetic interaction in addition to the  $\mu_4\text{-oxo}$  group, and so the model is oversimplified. Moreover, for this model, it can be observed that the ground state in

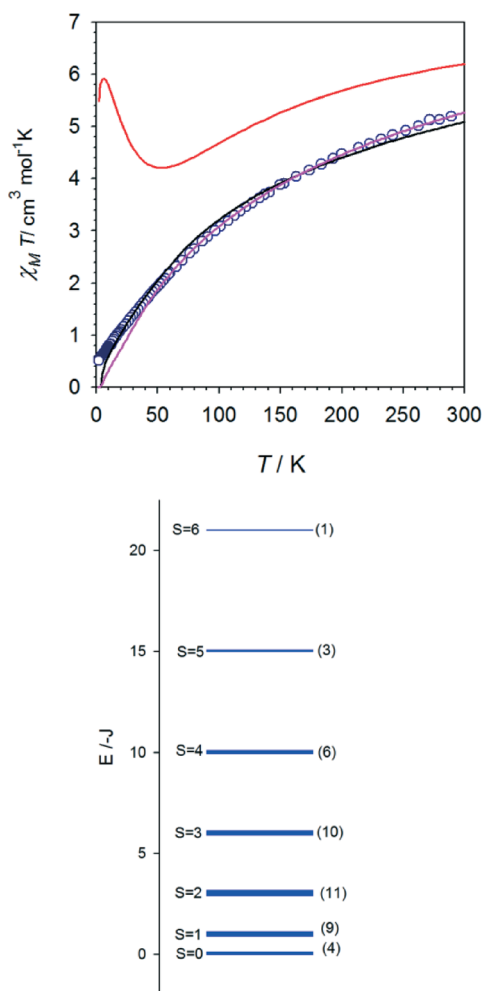


**Fig. 8** Temperature dependence of the  $\chi_M T$  product for complex **1**, blue circles. The black solid line is the theoretical plot for a tetrahedron with one magnetic coupling constant. The pink solid line is the theoretical plot considering two tetrahedra each with a different magnetic coupling constant. The red line corresponds to the theoretical model for a single tetrahedron with two different magnetic coupling constants. (b) Energy diagram for the spin states of the regular tetrahedron of spin quartets.

the case of antiferromagnetic interactions is  $S = 0$ , which exhibits a four-fold degeneracy. This means that on lowering the temperature, the magnetic moments of the cobalt(II) ions would cancel each other and the  $\chi_M T$  product should tend to zero. But the experimental magnetic susceptibility values do not tend to zero on lowering temperature, which is an additional deviation of the model.

A better approximation to the problem would consider magnetic interactions through the carboxylate and pyrazolate bridges, but without disorder in the pyrazolate–carboxylate linker. Therefore, 50% of the tetrahedra would be  $\{M_4(\mu_4-O)(pz)_6\}$ , and the other 50% would be  $\{M_4(\mu_4-O)(O_2C)_6\}$ . This way, we would have two different kinds of tetrahedra, each with a different magnetic coupling constant  $J_1$  and  $J_2$ . The expression for the magnetic susceptibility can be easily derived from eqn (3). The best-fit parameters for this model are  $J_1 = -13.29 \text{ cm}^{-1}$  and  $J_2 = -71.24 \text{ cm}^{-1}$ ,  $g = 2.18$  and  $R = 1.2 \times 10^{-4}$ .

This model gives a much better match for the theoretical plot, and the values of  $g$  and  $J_1$  and  $J_2$  seem reasonable. However, the theoretical curve deviates again at low temperatures since for this model, the ground state, and the only one populated at low temperatures, is again  $S = 0$ .

There are many magneto-structural studies which involve separately  $\mu$ -oxo, *syn-syn* carboxylate and pyrazolate bridges.<sup>45,47</sup> When they occur separately, *syn-syn* carboxylate and pyrazolate bridges mediate moderate antiferromagnetic coupling, and the  $\mu$ -oxo bridges also mediate antiferromagnetic interactions for angles larger than  $97^\circ$  (we have  $109.6^\circ$  in **1**).<sup>48</sup> However, there is a lack of magneto-structural studies in combined  $\mu_4$ -oxo + *syn-syn* carboxylate and  $\mu_4$ -oxo + pyrazolate bridges with Co(II) ions in tetrahedral surroundings, and just a few studies can be found for other cations such as Cu(II),<sup>49,50</sup> Ni(II)<sup>51</sup> or Co(II)<sup>52</sup> in octahedral surrounding. In those studies, antiferromagnetic interactions are found for large M–O–M angles,<sup>49,51</sup> which is the case of compound **1**. (Although ferromagnetic coupling is found for octahedral Co(II) ions with  $\mu_2$ -oxo + *syn-syn* carboxylate, the environment of the Co(II) ion is critical since the ground term for an octahedron is  $^4T_{1g}$  and that of a tetrahedron is  $^4A_2$ . This implies a different location of the unpaired electrons and very different orbital angular momentum contribution.)<sup>52–54</sup> Moreover, antiferromagnetic interactions have been observed in other Co(II) compounds with very similar  $\mu_4$ -oxo + *syn-syn* carboxylate bridges, so antiferromagnetic interactions are expected.<sup>55,56</sup> However, we cannot assign unambiguously the values of  $J_1$  and  $J_2$  to any of the bridges.

The definitive model to study the magnetic properties of compound **1** should consider the disorder in the pyrazolate–carboxylate linker. This disorder causes the six edges of the metal tetrahedron to be randomly bridged by either the carboxylate or the pyrazolate groups, which leads to the occurrence of tetrahedra having, from six to zero and from zero to six, *syn-syn* carboxylate and pyrazolate bridges, respectively. The probability of each kind of tetrahedron is shown in Fig. 9. Of course, such a study is not feasible: we would need to solve separately the Hamiltonian (by diagonalizing the  $256 \times 256$  matrix) for each tetrahedron (15 in total), calculate the numerical expression for the susceptibility for each one and include them with their correct weight in a full expression to calculate  $J_1$  and  $J_2$  simultaneously. This full study is beyond our purpose, and probably, there are other compounds more simple to investigate the magnetic properties of cobalt(II) ions bridged by combined  $\mu_4$ -O and *syn-syn* carboxylate and pyrazolate bridges. Nevertheless, this analysis of the topology of the tetrahedra will allow us to understand why the  $\chi_M T$  product does not tend to zero at low temperatures, and we will explain it focusing on one of the  $\{Co_4(\mu_4-O)(pz)_3(O_2C)_3\}$  tetrahedra.

One of those  $\{Co_4(\mu_4-O)(pz)_3(O_2C)_3\}$  tetrahedra has one cobalt(II) ion with three *syn-syn* carboxylate bridges connecting this cobalt(II) ion with its three nearest neighbors (encircled in Fig. 9a). Let us assume that the coupling through this *syn-syn* carboxylate bridge is the strongest one with  $J_1 = -71.24 \text{ cm}^{-1}$ .

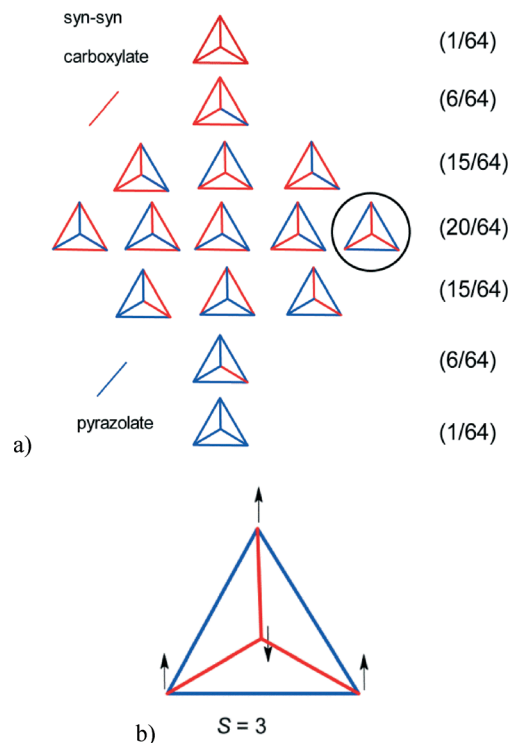


**Fig. 9** Statistic distribution of the randomly bridged  $\{\text{Co}_4(\mu_4\text{-O})(\text{pz}/\text{O}_2\text{C})_6\}$  tetrahedra. Blue edges correspond to pyrazolate bridges and red ones to *syn-syn* carboxylate. (b) The ground state  $S = 3$  is expected for the selected tetrahedron on the basis of the stronger antiferromagnetic coupling through the *syn-syn* carboxylate with respect to the pyrazolate bridge (which is frustrated). Other tetrahedra may also exhibit  $S \neq 0$  ground states or at least  $S \neq 0$  populated states at low temperatures.

As the coupling through this bridge is stronger than the coupling through the pyrazolate bridge, the former predominates, whereas the latter is frustrated, and the resulting situation leads to a  $S = 3$  ground state. As we have four vertices in a tetrahedron,  $4/64$  of the total of tetrahedra will have this arrangement, and so at least 6.25% of the clusters will not have a  $S = 0$  as ground state, and therefore, at low temperatures, the experimental  $\chi_{\text{M}}T$  product would not tend to zero. We can simulate the  $\chi_{\text{M}}T$  product for other tetrahedra, and we can see that only the two with all six magnetic coupling identical have a  $\chi_{\text{M}}T$  product which tends to zero; all the rest tend to positive values, so the positive value of the  $\chi_{\text{M}}T$  product at low temperatures is a consequence of the disorder in the linker. On the other hand, compounds with similar structure and with just one kind of bridge have experimental  $\chi_{\text{M}}T$  plots which tend to zero.<sup>54</sup>

## Conclusions

In summary, we have presented here four isostructural Metal-Azolate-Carboxylate (MAC) frameworks based on  $\{\text{M}_4(\mu_4\text{-O})\}$  nodes ( $\text{M} = \text{Co}, \text{Zn}$ ) with ligands combining a pyrazolate and carboxylate functionality at two different lengths. The four MACs feature the cubic *pcu-a* topology as in MOF-5 and

analogous IRMOFs. The Zn frameworks are stable in water-DMF mixtures for at least one hour. Small pore apertures and inner BET surface areas  $<1000 \text{ m}^2 \text{ g}^{-1}$  in the MACs with the short 3,5-dimethyl-pyrazolate-4-carboxylate ligand still yield a  $\text{H}_2$  and  $\text{CO}_2$  uptake, higher than MOF-5 with three times BET surface area. The compounds are thermally stable up to 350–400 °C. The antiferromagnetic coupling observed for **1** arises from the interactions of the cobalt(II) ions through the combined  $\mu_4\text{-O} + \text{syn-syn}$  carboxylate and  $\mu_4\text{-O} + \text{pyrazolate}$  bridges.

## Experimental section

Synthesis and spectroscopic analysis details of the ligands and compounds **1–4** are given in the ESI.†

### Powder X-ray diffraction (PXRD) measurements

Powder X-ray diffraction (PXRD) measurements were carried out on samples at ambient temperature with a Bruker D2 Phaser using a flat silicon, low background sample holder and  $\text{Cu-K}\alpha$  radiation ( $\lambda = 1.54184 \text{ \AA}$ ) at 30 kV and  $0.04^\circ \text{ s}^{-1}$ . Simulated PXRD patterns were calculated from single-crystal data using the MERCURY 3.0.1 software suite from CCDC.

### Gas sorption measurements

Sorption isotherms were measured using a Micromeritics ASAP 2020 automatic gas sorption analyzer equipped with oil-free vacuum pumps (ultimate vacuum  $<10^{-8}$  mbar) and valves, which guaranteed contamination-free measurements.

For the sorption measurements, 30 to 100 mg of freshly synthesized samples were subjected to a solvent-removal procedure and were processed immediately afterwards. After filtration and washing with small amounts of the same solvent as used for synthesis, the samples were pre-dried at a vacuum of  $10^{-3}$  Torr and stored under nitrogen.

The dried samples were transferred to nitrogen-filled and pre-weighed sample tubes capped with a septum. The tube was immediately purged with nitrogen after the transfer and the solvent removed with a syringe and through drying in vacuum ( $\sim 10$  Torr), which was followed by a control weighing. Then the sample was connected to the preparation port of the sorption analyzer and degassed under vacuum until the outgassing rate, *i.e.*, the rate of pressure rise in the temporarily closed manifold with the connected sample tube was less than  $2 \mu\text{Torr min}^{-1}$  at the specified temperature (70–250 °C). Typically, the samples were degassed for over 24 h in a vacuum of  $10^{-5}$  to  $10^{-6}$  bar and 200 °C. No solvent exchange process was carried out before degassing (see below). After their synthesis, the samples were only washed with DMF or DEF.

According to the X-ray structural data (*cf.* Fig. 2), the pore openings in the isostructural compounds **1** and **2** are very narrow. Therefore, the traditional solvent exchange procedure, through soaking in a low-boiling solvent (like MeOH,  $\text{CH}_2\text{Cl}_2$ ), was regarded ineffective. Hence, activation of **1** and **2** was carried out by direct high-temperature degassing (see

above). Thermogravimetric analyses of **1** and **2** (Fig. S13 and S16,<sup>†</sup> respectively) revealed that complete loss of solvent guest molecules should be finished at temperatures of ~300–350 °C at atmospheric pressure. Samples of **1** were degassed at different temperatures in ~10<sup>-6</sup> bar vacuum, and the H<sub>2</sub> adsorption was measured in order to determine the optimum degassing conditions for both **1** and **2**. For **1** degassed at 190 °C, an adsorption of 145 cm<sup>3</sup> H<sub>2</sub> at STP (standard temperature and pressure) was found, at 220 °C, an H<sub>2</sub> adsorption of 188 cm<sup>3</sup> and at 250 °C of 193 cm<sup>3</sup> was obtained. TG analysis of a sample degassed at a temperature of 250 °C confirmed the complete removal of guest molecules, and this degassing condition was used for subsequent gas sorption measurements for both **1** and **2**.

After weighing, the sample tube was then transferred to the analysis port of the sorption analyzer. All used gases (H<sub>2</sub>, Ar, N<sub>2</sub>, CO<sub>2</sub>, CH<sub>4</sub>) were of ultra high purity (UHP, grade 5.0, 99.999%), and the STP volumes are given according to the NIST standards (293.15 K, 101.325 kPa). Helium gas was used for the determination of the cold and warm free space of the sample tubes. H<sub>2</sub> and N<sub>2</sub> sorption isotherms were measured at 77 K (liquid nitrogen bath), whereas CO<sub>2</sub> and CH<sub>4</sub> sorption isotherms were measured at 293 ± 1 K (passive thermostating) and 273.15 K (ice/deionized water bath). The determination of the heat of adsorption values using the Clausius–Clapeyron equation and the DFT calculations ('N<sub>2</sub> DFT slit pore' model) were done using the ASAP 2020 v3.05 software.

Some of the secondary measurements, specified in the description, were performed using a Quantachrome iQ MP or NOVA automatic sorption analyzer. The DFT calculations, e.g., for the pore size distribution curves were carried out using the native ASiQWin 1.2 software employing the N<sub>2</sub> at 77 K on carbon, slit pore, NLDFT equilibrium model.<sup>57–59</sup>

### Water stability tests

The water stability test performed here followed the procedure by Cychosz and Matzger.<sup>17</sup> Sample preparation was done using the same parameters and equipment as used in the literature procedure. For direct comparison, MOF-5 was synthesized by us<sup>14</sup> to assess its water stability in direct comparison. In the literature, the PXRD patterns of MOF-5 already indicate decomposition at a (v:v) water–DMF ratio of 1:2.<sup>17</sup>

### X-ray crystallography

Suitable single crystals were carefully selected under a polarizing microscope.

**Data collection.** Compound **1** and **2**: Super Nova A from Agilent Technologies with microfocus tube, Cu-K $\alpha$  radiation ( $\lambda = 1.54178 \text{ \AA}$ ), 293 ± 2 K;  $\omega$ -scans, mirror system. Data collection, cell refinement and data reduction with CrysAlisPro, experimental absorption correction using spherical harmonics, implemented in SCALE3 ABSPACK scaling algorithm.<sup>60</sup> Compound **3**: Bruker Kappa APEX2 CCD diffractometer with

Table 2 Crystal data and structure refinement

Compound	1	2	3
Empirical formula	C <sub>18</sub> H <sub>18</sub> Co <sub>4</sub> N <sub>6</sub> O <sub>7</sub> <sup>a</sup>	C <sub>18</sub> H <sub>18</sub> N <sub>6</sub> O <sub>7</sub> Zn <sub>4</sub> <sup>b</sup>	C <sub>36</sub> H <sub>30</sub> Co <sub>4</sub> N <sub>6</sub> O <sub>7</sub> <sup>c</sup>
<i>M</i> /g mol <sup>-1</sup>	666.11	691.87	884.30
Crystal size/mm	0.13 × 0.11 × 0.11	0.12 × 0.12 × 0.12	0.01 × 0.01 × 0.01
2 $\theta$ range/°	8.8–132.72	8.82–132.52	6.18–80.16
<i>h</i> ; <i>k</i> ; <i>l</i> ; range	-8,23; -4,16; -23,21	-15,11; -15,23; -21,16	±11, ±11, -10,11
Crystal system	Cubic	Cubic	Orthorhombic
Space group	<i>F</i> $\bar{4}3m$ (no. 216)	<i>F</i> $\bar{4}3m$ (no. 216)	<i>P</i> 222 (no. 16)
<i>a</i> /Å	20.1090(7)	20.071(3)	14.242(3)
<i>b</i> /Å	20.1090(7)	20.071(3)	14.278(3)
<i>c</i> /Å	20.1090(7)	20.071(3)	14.2332(4)
<i>V</i> /Å <sup>3</sup>	8131.5(5)	8085.4(18)	2914.5(12)
<i>Z</i>	8	8	1
<i>D</i> <sub>calc</sub> /g cm <sup>-3</sup>	1.088	1.137	0.504
<i>F</i> (000)	2656	2752	442
$\mu$ /mm <sup>-1</sup>	12.829	2.964	4.529
Max/min transmission	0.307/0.196	1.000/0.816	0.748/0.458
Reflection collected ( <i>R</i> <sub>int</sub> )	1559 (0.0354)	1275 (0.0425)	6548 (0.0890)
Data completeness/%	99.0	99.3	95.3
Independent reflections	641	604	1690
Parameters refined	54	54	130
Max/min $\Delta\rho^d$ / e Å <sup>-3</sup>	1.341/-0.668	0.47/-0.50	0.230/-0.159
<i>R</i> <sub>1</sub> / <i>wR</i> <sub>2</sub> [ <i>I</i> > 2 $\sigma$ ( <i>I</i> )] <sup>e</sup>	0.0723/0.2078	0.0376/0.0937	0.0691/0.1453
<i>R</i> <sub>1</sub> / <i>wR</i> <sub>2</sub> (all reflections) <sup>e</sup>	0.0814/0.2203	0.0491/0.0998	0.1120/0.1574
Goodness-of-fit on <i>F</i> <sup>2f</sup>	1.157	1.001	0.923
Weighting scheme <i>w</i> , <i>a</i> / <i>b</i> <sup>g</sup>	0.1464/0.0000	0.0450/0.0000	0.0914/0.000

<sup>a</sup> For **1**, a total of 860 electrons per 3100 Å<sup>3</sup> was squeezed, which corresponds to ~107 electrons per C<sub>18</sub>H<sub>18</sub>Co<sub>4</sub>N<sub>6</sub>O<sub>7</sub> formula unit (*Z* = 8). PLATON<sup>64</sup> calculates a total potential solvent area volume of 3182 Å<sup>3</sup> per unit cell volume of 8131.5 Å<sup>3</sup> (39.1%). <sup>b</sup> For **2**, a total of 812 electrons per 3688 Å<sup>3</sup> was squeezed, which corresponds to ~101 electrons per C<sub>18</sub>H<sub>18</sub>N<sub>6</sub>O<sub>7</sub>Zn<sub>4</sub> formula unit (*Z* = 8). PLATON<sup>64</sup> calculates a total potential solvent area volume of 3736.8 Å<sup>3</sup> per unit cell volume of 8085.0 Å<sup>3</sup> (46.2%). <sup>c</sup> For **3**, total of 749 electrons per 2107 Å<sup>3</sup> and formula unit (*Z* = 1) was squeezed. PLATON<sup>64</sup> calculates a total potential solvent area volume of 2088.6 Å<sup>3</sup> per unit cell volume of 2914.5 Å<sup>3</sup> (71.7%). <sup>d</sup> Largest difference peak and hole. <sup>e</sup>  $R_1 = [\sum(|F_o| - |F_c|)] / \sum |F_o|$ ;  $wR_2 = [\sum[w(F_o^2 - F_c^2)^2]] / \sum[w(F_o^2)^2]$ . <sup>f</sup> Goodness-of-fit =  $[\sum[w(F_o^2 - F_c^2)^2]] / (n - p)$ . <sup>g</sup>  $w = 1 / [\sigma^2(F_o^2) + (aP)^2 + bP]$ , where  $P = (\max(F_o^2 \text{ or } 0) + 2F_c^2) / 3$ .

microfocus tube. Cu-K $\alpha$  radiation ( $\lambda = 1.54178 \text{ \AA}$ ),  $95 \pm 2 \text{ K}$ , multi-layer mirror system,  $\omega$ - and  $\theta$ -scan. Data collection with APEX2,<sup>61</sup> cell refinement and data reduction with SAINT,<sup>61</sup> experimental absorption correction with SADABS.<sup>62</sup> Several crystallization experiments were performed both at room and low temperature to obtain single crystals of 3 of suitable large size. However, from these numerous attempts, only small-size crystals of about  $0.01 \times 0.01 \times 0.01 \text{ mm}$  could be obtained. Because of this small size of about  $0.01 \times 0.01 \times 0.01 \text{ mm}$  and the high absorption coefficient of Co atoms, the crystals did not diffract over a  $2\theta$  angle of  $75^\circ$ . For this reason, the  $2\theta$  angle was limited to  $80^\circ$  for the given measurement, which however caused Alert level A (value of  $\sin(\theta_{\text{max}})/\lambda$  is less than 0.550; maximum shift/error of 0.27) and Alert level B (low theta full of 0.953). The low diffracting power originates from the crystal size, guest molecules in the MOF cavities and disorder in the crystal. Generally, a combination of weak high-angle data and pores in the crystal is the reason for low X-ray data quality in MOF structures.

**Structure analysis and refinement.** Using Olex2<sup>63</sup> for 1 and 2, all three structures were solved by direct methods using SHELXS-97; refinement was done by full-matrix least squares on  $F^2$  using the SHELXL-97 program suite.<sup>64</sup> The crystal solvent in the voids of 1–3 was found to be highly disordered and could not be properly defined. Hence, the option SQUEEZE in PLATON for Windows<sup>65</sup> was used to refine the framework structure without the disordered electron density in the voids. All non-hydrogen positions in 1 and 2 were refined with anisotropic displacement parameters. Hydrogen atoms for CH- or CH<sub>3</sub> were positioned geometrically (C–H =  $1.00 \text{ \AA}$  for aliphatic CH, C–H =  $0.99 \text{ \AA}$  for CH<sub>2</sub>, C–H =  $0.98 \text{ \AA}$  for CH<sub>3</sub>) and refined using riding models (AFIX 83 for OH, AFIX 43 for NH, AFIX 13 for aliphatic CH, AFIX 23 for CH<sub>2</sub>, AFIX 33 or 137 for CH<sub>3</sub>) with  $U_{\text{iso}}(\text{H}) = 1.2 U_{\text{eq}}(\text{CH}, \text{CH}_2)$  and  $U_{\text{iso}}(\text{H}) = 1.5 U_{\text{eq}}(\text{CH}_3)$ .

For 3, only cobalt, oxygen and one of the nitrogen atoms (N1) were refined with anisotropic displacement parameters. Carbon atoms and nitrogen atoms N2 and N3 remained isotropic. One aromatic hydrogen atom CH- and all hydrogen atoms of the CH<sub>3</sub>-groups were positioned geometrically and refined using a riding model with the same prerequisites as above.

All three crystal structures were found to be disordered on several positions. Disordered atoms were refined using the PART command.

Structures 1 and 3 were refined as near racemic twins with batch scale factors (BASF) of 0.42(7) for 1 and 0.459(6) for 3.

Graphics were obtained with DIAMOND.<sup>66</sup> Crystal data and details on the structure refinement are given in Table 2. The structural data have been deposited with the Cambridge Crystallographic Data Center (CCDC numbers 937761–937763).

**Magnetic measurements.** Magnetic susceptibility measurements on polycrystalline samples were carried out in the temperature range 1.9–300 K by means of a Quantum Design SQUID magnetometer operating at 10 000 Oe. Diamagnetic corrections

of the constituent atoms were estimated from Pascal's constants. Experimental susceptibilities were also corrected for the magnetization of the sample holder.

## Acknowledgements

The work was supported by DFG grant Ja466/25-1. I. B. thanks the Alexander von Humboldt foundation for the post-doctoral fellowship (1135450 STP).

## Notes and references

- 1 Introductions to special MOF issues: J. R. Long and O. M. Yaghi, *Chem. Soc. Rev.*, 2009, **38**, 1213–1214; H.-C. Zhou, J. R. Long and O. M. Yaghi, *Chem. Rev.*, 2012, **112**, 673–674.
- 2 C. Janiak and J. K. Vieth, *New J. Chem.*, 2010, **34**, 2366–2388; S.-H. Jhung, N. A. Khan and Z. Hasan, *CrystEngComm*, 2012, **14**, 7099–7109.
- 3 (a) J.-R. Li, R. J. Kuppler and H.-C. Zhou, *Chem. Soc. Rev.*, 2009, **38**, 1477–1504; (b) M. Paik Suh, H. J. Park, T. K. Prasad and D.-W. Lim, *Chem. Rev.*, 2012, **112**, 782–835.
- 4 H. Wu, Q. Gong, D. H. Olson and J. Li, *Chem. Rev.*, 2012, **112**, 836–868; L. J. Murray, M. Dincă and J. R. Long, *Chem. Soc. Rev.*, 2009, **38**, 1294–1314.
- 5 (a) Z. Zhang, Y. Zhao, Q. Gong, Z. Li and J. Li, *Chem. Commun.*, 2013, **49**, 653–661; (b) H. B. Tanh Jeazet, C. Staudt and C. Janiak, *Dalton Trans.*, 2012, **41**, 14003–14027; (c) J.-R. Li, J. Sculley and H.-C. Zhou, *Chem. Rev.*, 2012, **112**, 869–932; (d) G. Férey, C. Serre, T. Devic, G. Maurin, H. Jobic, P. L. Llewellyn, G. De Weireld, A. Vimont, M. Daturif and J.-S. Chang, *Chem. Soc. Rev.*, 2011, **40**, 550–562; (e) J.-R. Li, Y. Ma, M. C. McCarthy, J. Sculley, J. Yu, H.-K. Jeong, P. B. Balbuena and H.-C. Zhou, *Coord. Chem. Rev.*, 2011, **255**, 1791–1823.
- 6 B. Zheng, H. Liu, Z. Wang, X. Yu, P. Yi and J. Bai, *CrystEngComm*, 2013, **15**, 3517–3520; Z.-M. Zhang, T.-Z. Zhang, Y. Lu, F. Hai and E.-B. Wang, *CrystEngComm*, 2013, **15**, 459–462; C. Hou, Q. Liu, T.-a. Okamura, P. Wang and W.-Y. Sun, *CrystEngComm*, 2012, **14**, 8569–8576; W.-Y. Gao, Y. Niu, Y. Chen, L. Wojtas, J. Cai, Y.-S. Chen and S. Ma, *CrystEngComm*, 2012, **14**, 6115–6117; C. Li, W. Qiu, W. Shi, H. Song, G. Bai, H. He, J. Li and M. J. Zaworotko, *CrystEngComm*, 2012, **14**, 1929–1932; M. Kim and S. M. Cohen, *CrystEngComm*, 2012, **14**, 4096–4104.
- 7 K. A. Cychosz, R. Ahmad and A. J. Matzger, *Chem. Sci.*, 2010, **1**, 293–302.
- 8 P. Horcajada, R. Gref, T. Baati, P. K. Allan, G. Maurin, P. Couvreur, G. Férey, R. E. Morris and C. Serre, *Chem. Rev.*, 2012, **112**, 1232–1268.
- 9 J.-Y. Lee, O. K. Farha, J. Roberts, K. A. Scheidt, S. T. Nguyen and J. T. Hupp, *Chem. Soc. Rev.*, 2009, **38**, 1450–1459; M. Yoon, R. Srirambalaji and K. Kim, *Chem. Rev.*, 2012, **112**, 1196–1231; J. Guo, J. Yang, Y.-Y. Liu and J.-F. Ma, *CrystEngComm*, 2012, **14**, 6609–6617; B. J. Burnett, P. M. Barron and W. Choe, *CrystEngComm*, 2012, **14**,

- 3839–3846; H.-j. Pang, H.-y. Ma, J. Peng, C.-j. Zhang, P.-p. Zhang and Z.-m. Su, *CrystEngComm*, 2011, **13**, 7079–7085.
- 10 F. Jeremias, V. Lozan, S. Henninger and C. Janiak, *Dalton Trans.*, 2013, DOI: 10.1039/c3dt51471d; C. Janiak and S. K. Henninger, *Chimia*, 2013, **67**, 419–424; C. Janiak and S. K. Henninger, *Nachr. Chem.*, 2013, **61**, 520–523; A. Khutia, H. U. Rammelberg, T. Schmidt, S. Henninger and C. Janiak, *Chem. Mater.*, 2013, **25**, 790–798; F. Jeremias, A. Khutia, S. K. Henninger and C. Janiak, *Eur. J. Inorg. Chem.*, 2012, 2625–2634; F. Jeremias, A. Khutia, S. K. Henninger and C. Janiak, *J. Mater. Chem.*, 2012, **22**, 10148–10151; J. Ehrenmann, S. K. Henninger and C. Janiak, *J. Mater. Chem.*, 2011, 471–474.
- 11 A. U. Czaja, N. Trukhan and U. Müller, *Chem. Soc. Rev.*, 2009, **38**, 1284–1293; G. Férey, *Dalton Trans.*, 2009, 4400–4415; M. J. Prakash and M. S. Lah, *Chem. Commun.*, 2009, 3326–3341.
- 12 M. Eddaoudi, J. Kim, N. Rosi, D. Vodak, J. Wachter, M. O’Keeffe and O. M. Yaghi, *Science*, 2002, **295**, 469–472.
- 13 I. Boldog, L. Xing, A. Schulz and C. Janiak, *C. R. Chim.*, 2012, **15**, 866–877; E. V. Alexandrov, V. A. Blatov, A. V. Kochetkov and D. M. Proserpio, *CrystEngComm*, 2011, **13**, 3947–3958.
- 14 S. S. Kaye, A. Dailly, O. M. Yaghi and J. R. Long, *J. Am. Chem. Soc.*, 2007, **129**, 14176–14177; H. Li, M. Eddaoudi, M. O’Keeffe and O. M. Yaghi, *Nature*, 1999, **402**, 276–279.
- 15 S. S. Han, S.-H. Choi and A. C. T. van Duin, *Chem. Commun.*, 2010, **46**, 5713–5715.
- 16 J. J. Low, A. I. Benin, P. Jakubczak, J. F. Abrahamian, S. A. Faheem and R. R. Willis, *J. Am. Chem. Soc.*, 2009, **131**, 15834–15842.
- 17 K. A. Cychoz and A. J. Matzger, *Langmuir*, 2010, **26**, 17198–17202.
- 18 V. Guillermin, F. Ragon, M. Dan-Hardi, T. Devic, M. Vishnuvarthan, B. Campo, A. Vimont, G. Clet, Q. Yang, G. Maurin, G. Férey, A. Vittadini, S. Gross and C. Serre, *Angew. Chem., Int. Ed.*, 2012, **51**, 9267–9271.
- 19 X.-C. Huang, Y.-Y. Lin, J.-P. Zhang and X.-M. Chen, *Angew. Chem., Int. Ed.*, 2006, **45**, 1557–1559; K. S. Park, Z. Ni, A. P. Côté, J. Y. Choi, R. Huang, F. J. Uribe-Romo, H. K. Chae, M. O’Keeffe and O. M. Yaghi, *Proc. Natl. Acad. Sci. U. S. A.*, 2006, **103**, 10186–10191.
- 20 G. Férey, C. Mellot-Draznieks, C. Serre, F. Millange, J. Dutour, S. Surble and I. Margiolaki, *Science*, 2005, **309**, 2040–2042.
- 21 J. H. Cavka, S. Jakobsen, U. Olsbye, N. Guillou, C. Lamberti, S. Bordiga and K. P. Lillerud, *J. Am. Chem. Soc.*, 2008, **130**, 13850–13851.
- 22 I. Boldog, K.V. Domasevitch, I. A. Baburin, H. Ott, B. Gil-Hernández, J. Sanchiz and C. Janiak, *CrystEngComm*, 2013, **15**, 1235–1243; H. J. Choi, M. Dincă, A. Dailly and J. R. Long, *Energy Environ. Sci.*, 2010, **3**, 117–123.
- 23 J.-P. Zhang, Y.-B. Zhang, J.-B. Lin and X.-M. Chen, *Chem. Rev.*, 2012, **112**, 1001–1033; M. A. Halcrow, *Dalton Trans.*, 2009, 2059–2073.
- 24 V. Colombo, C. Montoro, A. Maspero, G. Palmisano, N. Masciocchi, S. Galli, E. Barea and J. A. R. Navarro, *J. Am. Chem. Soc.*, 2012, **134**, 12830–12843; N. Masciocchi, S. Galli, V. Colombo, A. Maspero, G. Palmisano, B. Seyyedi, C. Lamberti and S. Bordiga, *J. Am. Chem. Soc.*, 2010, **132**, 7902–7904.
- 25 M. Tonigold, Y. Lu, A. Mavrandonakis, S. Puls, R. Staudt, J. Maellmer, J. Sauer and D. Volkmer, *Chem.–Eur. J.*, 2011, **17**, 8671–8695.
- 26 N. M. Padial, E. Quartapelle Procopio, C. Montoro, E. López, J. E. Oltra, V. Colombo, Maspero, N. Masciocchi, S. Galli, I. Senkovska, S. Kaskel, E. Barea and J. A. R. Navarro, *Angew. Chem.*, 2013, **125**, 8448–8452.
- 27 D. J. Tranchemontagne, K. S. Park, H. Furukawa, J. Eckert, C. B. Knobler and O. M. Yaghi, *J. Phys. Chem. C*, 2012, **116**, 13143–13151.
- 28 W.-Y. Gao, W. Yan, R. Cai, L. Meng, A. Salas, X.-S. Wang, L. Wojtas, X. Shi and S. Ma, *Inorg. Chem.*, 2012, **51**, 4423–4425.
- 29 C.-T. He, J.-Y. Tian, S.-Y. Liu, G. Ouyang, J.-P. Zhang and X.-M. Chen, *Chem. Sci.*, 2013, **4**, 351–356.
- 30 J. Lincke, D. Lässig, M. Kobalz, J. Bergmann, M. Handke, J. Möllmer, M. Lange, C. Roth, A. Möller, R. Staudt and H. Krautscheid, *Inorg. Chem.*, 2012, **51**, 7579–7586.
- 31 C. Montoro, F. Linares, E. Quartapelle Procopio, I. Senkovska, S. Kaskel, S. Galli, N. Masciocchi, E. Barea and J. A. R. Navarro, *J. Am. Chem. Soc.*, 2011, **133**, 11888–11891.
- 32 A. Bétard, S. Wannapaiboon and R. A. Fischer, *Chem. Commun.*, 2012, **48**, 10493–10495.
- 33 A. Bhunia, V. Vasylyeva and C. Janiak, *Chem. Commun.*, 2013, **49**, 3961–3963.
- 34 S. Henke and R. A. Fischer, *J. Am. Chem. Soc.*, 2011, **133**, 2064–2067.
- 35 S. S. Mondal, A. Bhunia, I. A. Baburin, C. Jäger, A. Kelling, U. Schilde, G. Seifert, C. Janiak and H.-J. Holdt, *Chem. Commun.*, 2013, **49**, 7567–7570.
- 36 S. Yang, X. Lin, A. J. Blake, G. S. Walker, P. Hubberstey, N. R. Champness and M. Schröder, *Nat. Chem.*, 2009, **1**, 487–493.
- 37 K. Sumida, D. L. Rogow, J. A. Mason, T. M. McDonald, E. D. Bloch, Z. R. Herm, T.-H. Bae and J. R. Long, *Chem. Rev.*, 2012, **112**, 724–781.
- 38 A. J. Fletcher, E. J. Cussen, T. J. Prior, M. J. Rosseinsky, C. J. Kepert and K. M. Thomas, *J. Am. Chem. Soc.*, 2001, **123**, 10001–10011; E. J. Cussen, J. B. Claridge, M. J. Rosseinsky and C. J. Kepert, *J. Am. Chem. Soc.*, 2002, **124**, 9574–9581.
- 39 S.-i. Noro, S. Kitagawa, T. Akutagawa and T. Nakamura, *Prog. Polym. Sci.*, 2009, **34**, 240–279; S. Kitagawa and R. Matsuda, *Coord. Chem. Rev.*, 2007, **251**, 2490–2509.
- 40 C. Graham, D. A. Imrie and R. E. Raab, *Mol. Phys.*, 1998, **93**, 49–56.
- 41 K. A. Cychoz, A. G. Wong-Foy and A. J. Matzger, *J. Am. Chem. Soc.*, 2008, **130**, 6938–6939.
- 42 M. Kurmoo, *Chem. Soc. Rev.*, 2009, **38**, 1353–1379; D. Maspoth, D. Ruiz-Molina and J. Veciana, *Chem. Soc. Rev.*, 2007, **36**, 770–818; D. Maspoth, D. Ruiz-Molina and J. Veciana, *J. Mater. Chem.*, 2004, **14**, 2713–2723; S. R. Batten and K. S. Murray, *Coord. Chem. Rev.*, 2003, **246**, 103–130; C. Janiak, *Dalton Trans.*, 2003, 2781–2804.
- 43 J. K. Maclaren, J. Sanchiz, P. Gili and C. Janiak, *New J. Chem.*, 2012, **36**, 1596–1609; B. Gil-Hernández, J. K. Maclaren,

- H. A. Höpfe, J. Pasan, J. Sanchiz and C. Janiak, *CrystEngComm*, 2012, **14**, 2635–2644; B. Gil-Hernández, H. Höpfe, J. K. Vieth, J. Sanchiz and C. Janiak, *Chem. Commun.*, 2010, **46**, 8270–8272; B. Gil-Hernández, P. Gili, J. K. Vieth, C. Janiak and J. Sanchiz, *Inorg. Chem.*, 2010, **49**, 7478–7490; H. A. Habib, J. Sanchiz and C. Janiak, *Inorg. Chim. Acta*, 2009, **362**, 2452–2460; H. A. Habib, J. Sanchiz and C. Janiak, *Dalton Trans.*, 2008, 4877–4884; H. A. Habib, J. Sanchiz and C. Janiak, *Dalton Trans.*, 2008, 1734–1744.
- 44 T. Gao, X.-Z. Wang, H.-X. Gu, Y. Xu, X. Shen and D.-R. Zhu, *CrystEngComm*, 2012, **14**, 5905–5913; S.-Q. Guo, D. Tian, X. Zheng and H. Zhang, *CrystEngComm*, 2012, **14**, 3177–3182; J.-Q. Liu, Y.-Y. Wang, T. Wu and J. Wu, *CrystEngComm*, 2012, **14**, 2906–2913.
- 45 O. Kahn, *Molecular Magnetism*, VCH, New York, 1993.
- 46 D. Nelson and W. Haar, *Inorg. Chem.*, 1993, **32**, 182–188.
- 47 J. Olguín, M. Kalisz, R. Clérac and S. Brooker, *Inorg. Chem.*, 2012, **51**, 5058–5069.
- 48 V. H. Crawford, H. W. Richardson, J. R. Wasson, D. J. Hodgson and W. E. Hatfield, *Inorg. Chem.*, 1976, **15**, 2107–2110.
- 49 S. Ferrer, F. Lloret, I. Bertomeu, G. Alzuet, J. Borrás, S. García-Granada, M. Liu-González and J. G. Haasnoot, *Inorg. Chem.*, 2002, **41**, 5821–5830.
- 50 S. Ferrer, F. Lloret, E. Pardo, J. M. Clemente-Juan, M. Liu-González and S. García-Granda, *Inorg. Chem.*, 2012, **51**, 985–1001.
- 51 J. Ruiz, A. J. Mota, A. Rodríguez-Diéguez, I. Oyarzabal, J. M. Seco and E. Colacio, *Dalton Trans.*, 2012, **41**, 14265–14273.
- 52 H. Arora, S. K. Barman, F. Lloret and M. Mukherjee, *Inorg. Chem.*, 2012, **51**, 5539–5553.
- 53 S. M. Ostrovsky, K. Falk, J. Pelikan, D. A. Brown, Z. Tomkowicz and W. Haase, *Inorg. Chem.*, 2006, **45**, 688–694.
- 54 F. Lloret, J. Julve, J. Cano, R. Ruiz-García and E. Pardo, *Inorg. Chim. Acta*, 2008, **361**, 3432–3445.
- 55 P. Jaitner, J. Veciana, C. Sporer, H. Kopacka, K. Wurst and D. Ruiz-Molina, *Organometallics*, 2001, **20**, 568–571.
- 56 A. B. Blake, *Chem. Commun.*, 1966, 569.
- 57 L. D. Gelb, K. E. Gubbins, R. Radhakrishnan and M. Sliwinska-Bartowiak, *Rep. Prog. Phys.*, 1999, **62**, 1573–1659.
- 58 N. A. Sedron, J. P. R. B. Walton and N. Quirke, *Carbon*, 1989, **27**, 853–861.
- 59 A. Vishnyakov, P. Ravikovitch and A. V. Neimark, *Langmuir*, 2000, **16**, 2311–2320.
- 60 CrysAlisPro, Agilent Technologies, Version 1.171.36.2 (release 08-11-2011 CrysAlis171.NET).
- 61 Apex2, Data Collection Program for the CCD Area-Detector System; SAINT, Data Reduction and Frame Integration Program for the CCD Area-Detector System., Bruker Analytical X-ray Systems, Madison, Wisconsin, USA, 1997–2006.
- 62 G. Sheldrick, Program SADABS: Area-detector absorption correction, University of Göttingen, Germany, 1996.
- 63 OLEX2: a complete structure solution, refinement and analysis program O. V. Dolomanov, L. J. Bourhis, R. J. Gildea, J. A. K. Howard and H. Puschmann, *J. Appl. Crystallogr.*, 2009, **42**, 339–341.
- 64 G. M. Sheldrick, *Acta Crystallogr. A*, 2008, **64**, 112–122.
- 65 A. L. Spek, *J. Appl. Crystallogr.*, 2003, **36**, 7–13; PLATON – A Multipurpose Crystallographic Tool, Utrecht University, Utrecht, The Netherlands, A. L. Spek, 2008; Windows implementation: L. J. Farrugia, University of Glasgow, Scotland, Version 40608, 2008.
- 66 K. Brandenburg, Diamond (Version 3.2), crystal and molecular structure visualization, Crystal Impact. K. Brandenburg & H. Putz Gbr, Bonn, Germany, 2007–2012.